PASJ: Publ. Astron. Soc. Japan , 1–??,

Wavelength Determination for Solar Features Observed by the EUV Imaging Spectrometer on Hinode

C. M. Brown
Space Science Division, Naval Research Laboratory, Washington DC 20375, USA
cbrown@ssd5.nrl.navy.mil
H. Hara, S. Kamio
National Astronomical Observatory, Mitaka, Tokyo 181-8588
hirohisa.hara@nao.ac.jp suguru.kamio@nao.ac.jp
U. Feldman
Artep, Inc., Ellicott City, MD 21047, USA
ufeldman@ssd5.nrl.navy.mil
J. F. Seely, G. A. Doschek, J. T. Mariska, C. M. Korendyke
Space Science Division, Naval Research Laboratory, Washington DC 20375, USA
jseely@ssd5.nrl.navy.mil gdoschek@ssd5.nrl.navy.mil
mariska@nrl.navy.mil ckorendyke@ssd5.nrl.navy.mil
J. Lang
Rutherford Appleton Laboratory, Chilton, Didcot, Oxon OX11 0QX UK
J.Lang@rl.ac.uk
K. Dere
George Mason University, 4400 University Drive, Fairfax, VA 22020, USA
kdere@gmu.edu
J. L. Culhane
Mullard Space Science Laboratory, University College London, Holmbury St. Mary, Dorking, Surrey, RH5 6NT, UK
jlc@mssl.ucl.ac.uk
R. J. Thomas, and J. M.Davila
NASA Goddard Space Flight Center, Greenbelt, MD 20771, USA
Roger.J.Thomas@nasa.gov Joseph.M.Davila@nasa.gov

(Received 2007 June 13; accepted 2007 August 21)

Abstract

A wavelength calibration of solar lines observed by the high resolution EUV Imaging Spectrometer (EIS) on the Hinode satellite is reported. Spectral features of the quiet sun and of two mildly active areas were measured and calibrated. A listing of the stronger observed lines with identification of the leading contributor ions is presented. 41 lines are reported, with 90% identified. Wavelength precisions (2σ) of ± 0.0031 Å for the EIS short band and ± 0.0029 Å for the EIS long band are obtained. These lines, typical of $1 - 2 \times 10^6$ K plasmas, are recommended as standards for the establishment of EIS wavelength scales. The temperature of EIS varies by about 1.5° C around the orbit and also with spacecraft pointing. The correlation of these temperature changes with wavelength versus pixel number scale changes is reported.

Key words: Sun — Sun: UV radiation

1. Introduction

The Extreme Ultraviolet Imaging Spectrometer (EIS) on the Hinode (Kosugi et al., 2007) satellite is a high performance stigmatic instrument for observing the sun in the 170 Å – 210 Å and 246 Å – 290 Å regions (Korendyke et al., 2006; Culhane et al., 2007). The wavelength ranges were chosen because they contain a number of useful spectral lines for solar plasma diagnostics covering a range of temperatures from the upper transition region to that of solar flares. Two CCD detectors cover these two ranges with a nominal plate scale of 1″ per pixel and a dispersion of 0.0223 Å/pixel. EIS has four slits, 1″, 2″, 40″, and 266″ in width. The 1″ silt was selected for the present work.

The excellent pointing stability (about 0.4 arcsec/min at the 3σ level) of the Hinode spacecraft combines with the instrument resolution to permit stigmatic imaging with high fidelity, fast cadence, and calibrated sensitivity (Lang et al., 2006).

There are four CCD readout ports on EIS, each is 1024 columns wide and each has a different background level. In processing the spectrum, the minimum value (in data numbers, DN) was subtracted from the data from each readout port. The effects of hot pixels and cosmic rays were removed by passing the data through the SolarSoft CLEAN_EXPOSURE routine (Freeland, Handy, 1998). This routine detects and removes data points that vary

excessively from the average value of a box of surrounding pixels. For line spectra from the 1″ slit, the box size was set to 1×7 pixels. A high pixel value in the center of the box is replaced by the average of the remaining pixels. To avoid degrading the spectral resolution, the box was kept to the minimum in the spectral dimension. Since cosmic rays can create isolated pixels with very high values, this step is essential to good measurements.

2. Observations

Spectral data for this calibration were recorded on 4 November 2006 during the commissioning of the EIS instrument on orbit. Spectra were obtained in a 600 s exposure and recorded on the two CCDs. The short wave (SW) band was mapped onto pixel columns numbered 0 – 2047 and the long wave (LW) band onto 2048 – 4095. The lower half (rows 0 – 511) of the CCD was selected, and three typical strips were averaged along the spectral line to produce the three spectra measured here. Figure 1 is a short section of this stigmatic spectrum showing the three regions selected for averaging. For the quiet sun (QS), an 80″ region was selected, and for the two active areas (AR1, AR2), 20″ regions were averaged.

The selected rows for the three regions were each summed along columns and a spectrum of the average DN per pixel generated. These spectra were measured in pixel units using the GFit program (Engstrom, 1998) to fit Gaussian shapes to the line profiles. The sprctra were fitted in sections of about 50 to 70 columns (1 Å – 1.5 Å) at a time, each containing several lines. For each line, the peak position(in pixels), line full-width at half-maximum (FWHM), and Gaussian area (in DN) were reported. The local apparent background was also fitted and subtracted. This background includes the noise, continuum, faint unresolved lines, and the far wings of the non-Gaussian components of stronger lines. Well exposed unblended lines had a Gaussian FWHM of approximately 0.06 Å and those with areas larger than 200 DN have good precision. In the active regions, a few of the strongest lines were saturated in the 600 s exposure, but their wavelength precision is not noticeably affected.

3. Standard Lines and Fitting

To establish a wavelength scale, standard lines measured as above having a normal line width and appearance were selected. The solar wavelengths from Behring et al. (1976) were matched to measured features and fitted by least squares to a second order polynomial. No improvement was gained by using higher order polynomials. Each CCD was fitted separately, and different strips (row numbers) could be fitted by adjusting the λ_0 value of the polynomial slightly (< 10 mÅ) to account for the small amount of slit tilt. The slit tilt is very small for EIS, but is appreciable if one uses the full height of the slit image. It arises from the practical impossibility of perfectly aligning the CCD columns with the slit image. The residual tilt is on the order of one pixel in 200 rows, but is effectively removed in our wavelength calibration by the least-squares fitting wherein each measured strip is fitted separately to the wavelength standards. Likewise, the effects of the orbital variation of the wavelengths with temperature (see below) are removed by our procedure.

Table 1. Fitting Constants for SW and LW CCD's for AR2.

	λ_0 (Å)	α (Å /pixel)	β (Å /pixel^2)
SW CCD	166.1445	0.022299	-6.530E-9
σ coeff	0.0014	2.77E-6	1.19E-9
σ fit	0.00154		
LW CCD	199.9719	0.022316	-1.112E-8
σ coeff	0.0132	9.50E-6	1.625E-9
σ fit	0.00146		

The data for area AR2 are from CCD rows 269–288 (SW) and 256–275 (LW). σ coeff is the standard error of the coefficients λ_0, α, and β. σ fit is the standard error of the fit of the lines to the regression equations.

It is important to note that the Behring et al. measurements are solar observations and not laboratory wavelengths. For some lines, their precision surpasses that of laboratory measurements. This can be attributed in part to the fact that the reference solar lines were measured in second order (LW CCD range) and third order (SW CCD range) against accurate standards in the first order (500 Å – 600 Å).

We were able to slightly improve a few of the Behring et al. standards in such a way that they give better agreement with the visible coronal lines corresponding to transitions within the ground configurations of Si X, Fe XIII and Fe XIV. Specifically, the Fe XIII 204.942Å wavelength was changed to 204.937Å, so that its energy difference with the Fe XIII 201.121Å line corresponds to $9259 cm^{-1}$, the energy of a Fe XIII coronal line. The Fe XIV 270.524Å wavelength was changed to 270.519Å so that its energy difference, when compared to the Fe XIV 257.392Å will be $18853 cm^{-1}$, the energy of a Fe XIV coronal line. Similarly, we modified the 253.795Å and 258.373Å to 253.791Å and 258.375Å to agree with the Si X coronal line at $6990.6 cm^{-1}$. Two other Si X lines, 261.056 and 271.992 Å were adjusted by 0.002 Å to give better agreement with the nearby grade A lines of Behring et al. The revised standards are given in italics in Table 2.

The polynomial dispersion functions fitted were of the form:

$$\lambda(x) = \lambda_0 + \alpha x + \beta x^2 \qquad (1)$$

where x is the pixel column number of the line center. Table 1 summarizes the least squares coefficients and standard errors of the fitting process. Comparing the in-flight wavelength calibration with the pre-launch laboratory calibration (and accounting for the different pixel numbering schemes) shows a net shift of only 7 – 8 pixels in the spectra due to the combined effects of transportation, vibration testing, thermal-vacuum testing, and launch.

Figure 2 is a scattergram showing the residuals for a

Table 2. EIS Wavelength Measurement[a]

		Gaussian Area							
FWHM (Å)	Peak Pixel No.	QS (DN)	AR1 (DN)	AR2 (DN)	Standard λ(Å)	Ion	Grade	Fitted λ (Å)	Deviation (mÅ)
Short Waveband									
0.060	221.024	62	213	255	171.073	Fe IX	B	171.073	−0.2
0.061	376.177	174	848	652	174.532	Fe X	A	174.532	−0.1
0.052	408.883	25		96	175.263	Fe X	B	175.261	−2.0
0.062	497.564	210	1403	1085	177.239	Fe X	A	177.238	−1.0
0.067	534.350	28	288	111	178.056	Fe XI	B	178.058	2.0
0.067	639.465	1495	10633	5724	180.401	Fe XI	A	180.401	0.1
0.063	718.672	525	4714	2049	182.167	Fe XI	A	182.167	−0.3
0.060	825.044	1724	9322	6886	184.536	Fe X	A	184.538	1.5
0.061	990.076	6625	52280[b]	25526	188.216	Fe XI	A	188.216	−0.4
0.063	993.868	4462	32543	17272	188.299		A	188.300	1.1
0.065	1002.625	1644	6107	6637	188.493		B	188.495	2.3
0.077	1030.880	515	5963	1940	189.123	*Fe XI*	B	189.125	2.0
0.065	1071.887	2255	10182	8666	190.038	Fe X	A	190.039	0.8
0.062	1177.549	5544	58716[b]	21662	192.394	Fe XII	A	192.393	−0.6
0.066	1196.315	3454	21356	13338	192.813	Fe XI	B	192.812	−1.5
0.066	1227.540	13817	92764[b]	51691[b]	193.509	Fe XII	A	193.507	−1.7
0.096	1299.878	20626	114881[b]	78938[b]	195.119	Fe XII	A	195.119	0.2
0.071	1519.745	1559	20686	6584	200.021	Fe XIII	B	200.018	−3.1
0.078	1569.136	2296	32284	9360	201.121	Fe XII, Fe XIII	B B2x	201.118	−2.7
0.064	1610.735	4268	39495	16230	202.044	Fe XIII	A	202.045	1.0
0.069	1740.604	159	2516	703	*204.937*	Fe XIII	B	204.938	1.1
0.062	1853.304	111	641	407	207.449		B	207.449	−0.5
0.064	1964.149	103	951	419	209.916	Fe XIII	B	209.917	1.5
0.068	2026.961	448	7169	2145	211.316	Fe XIV	B	211.316	0.5
Long Waveband									
0.067	2074.032	153	2494	579	246.208	Fe XIII	B	246.208	0.1
0.070	2332.007	457	6963	1750	251.953	Fe XIII	B	251.952	−0.5
0.073	2342.940	147	2573	567	252.197	Fe XIV	B	252.196	−1.1
0.066	2414.627	108	1938	412	*253.791*	Si X	B	253.792	0.8
0.084	2544.530	222	201	1034	256.686	S XIII	B	256.684	−2.4
0.068	2555.462	311	2818	1255	256.925	*Fe XII*	A	256.927	1.9
0.079	2576.378	242	5295	1360	*257.390*	Fe XIV	A	257.392	2.5
0.061	2593.433	124	1453	476	257.772		B	257.772	0.1
0.074	2620.503	876	13971	3872	*258.375*	Si X	A	258.375	−0.4
0.075	2741.059	507	6203	1954	*261.058*	Si X	B	261.058	−0.2
0.071	2827.574	402	4892	1531	262.984	Fe XVI	A	262.983	−0.9
0.074	2883.843	279	4341	1285	264.233	S X	B B3x	264.235	2.2
0.069	2908.563	1791	33997	6711	264.787	Fe XIV	A	264.785	−1.7
0.073	3166.260	1067	18249	4019	*270.519*	Fe XIV	B	270.518	−0.5
0.078	3232.410	666	7564	2557	*271.990*	Si X	B	271.990	0.1
0.066	3331.941	2434	34784	8050	274.203	Fe XIV	B	274.204	1.0
0.077	3779.667	4281	47001	16266	284.160	Fe XV	B	284.160	0.0

[a] Standard wavelengths and quality grades are from Behring et al. (1976). The grade A=±0.002 Å, the grade B=±0.004 Å. B2X = blended with 2nd order etc. Data given in italics are revised wavelengths and identifications.

[b] Line is saturated in the AR 600 s exposure. Peak position is normal.

least squares fitting of the AR2 data to Behring et al. wavelengths. Only lines classified "A" or "B" (±0.002 Å or ±0.004 Å , respectively) in the Behring et al. line list were used. Weak, broadened, blended or partially resolved lines were not used for calibration. Using these calibrations and standards, wavelengths of unblended lines could be determined for EIS to ±0.002 Å, permitting accurate velocity and Doppler shift determinations. Table 2 is a listing of the select standard lines as measured in AR2 along with their Gaussian fitted areas from QS and AR1. Identifications and reference wavelengths are from Behring et al., with minor adjustments as noted above.

4. Orbital Variation

For optimal solar viewing, Hinode is in a sun-synchronous polar orbit. The spacecraft is three-axis stabilized with its Y axis aligned approximately with the solar north direction and its Z axis sunward. EIS is mounted on the +Y side of Hinode. This means that the ±X and +Y facing external surfaces of EIS see alternately the warm (∼220 K) earth and the cold (∼4 K) deep space in phase with Hinode's orbital motion. This drives small cyclic temperature variations on the order of 1 - 1.5° C within EIS and associated wavelength variations at the CCD. For high precision wavelength determinations, these variations must be accounted for.

As an example of this variation, Figure 3 is a plot of the variation found in the centroid of a Gaussian fitted to the Fe XII 195.12 Å line over five orbits. All other strong lines (e.g. 284 Å of Fe XV, 274 Å of Fe XIV and 202 Å of Fe XIII) exhibit a similar sinusoidal variation of their line centers. Plotted above on the same time scale is the temperature from a sensor mounted to the EIS grating assembly. Depending on the orbital phase, two exposures differing in time by as little as 10 minutes can have an appreciable wavelength shift. Likewise, long exposures such as our 600s exposure of 4 November 2006 can exhibit slightly increased line widths, depending on the phase of the orbit.

As a further example, Figure 4 shows a longer term line center variation associated with EIS temperature with the regular sinusoidal variation superimposed. At about 1100 UT on 6 December 2006, temperatures in the grating area began cooling as Hinode was repointed from the west limb to the east limb of the sun (see Figure 5). The orbital average centroid of the Fe XII 195 Å feature drifted upwards by 0.2 pixel (0.0045 Å), equivalent to 7 km/s in velocity. Long term variations in EIS temperature are caused by changes in Hinode pointing, EIS heater cycles, observational power consumption, and seasonal variations of the orbit.

A month long record of EIS grating temperatures is shown in Figure 5 for December, 2006, which shows the cooling mentioned above. The individual orbit swings are enveloped in this figure. The drifts in the general temperature profile are related to the Hinode pointing. On 6 December, Hinode began an observing campaign to track an active region from the east limb to the west limb of the sun. At the outset, a sharp drop of about 1.5° C was observed at the grating. Hinode continued to point at this active region as it crossed the disk to the west limb on 20 December. During this time, the average EIS grating area temperatures steadily rose by a total of about 2° C. Normal pointing operations with varied targets resumed after 20 December 2006.

5. Conclusions

EIS has proved itself to be a powerful, sensitive instrument for observing solar spectra in the difficult EUV region. It has unprecedented spatial, temporal and spectral resolution in this range. Where line statistics permit, line centroids and widths can be determined to 0.1 pixel or 0.002 Å (2-4 km/s, depending on the wavelength). The connection of small wavelength shifts to small temperature changes in EIS around the orbit is normal and has been established. A select set of well determined spectral lines from EIS is presented for use as standards in wavelength calibrating EIS and tracking wavelength shifts during studies. Where the best wavelengths are required, it is recommended that several of the lines from Table 2 from the same degree of ionization of the same atom or from ions with the same temperature of formation be included to allow the user to remove instrumental thermal shifts of wavelength.

Hinode is a Japanese mission developed and launched by ISAS/JAXA, with NAOJ as domestic partner and NASA and STFC (UK) as international partners. It is operated by these agencies in co-operation with ESA and NSC (Norway).

References

Behring, W., Cohen, L., Feldman, U., Doschek, G. A. 1976, ApJ, 203, 527

Culhane, J. L., Harra, L. K., James, A. M., *et al.* 2007, Sol. Phys., in press

Engstrom, L. 1998, PROGRAM GFit v 10.0 (05-05-19), Lund Reports on Atomic Physics, LRAP-232 Available online at: *http://kurslab-atom.fysik.lth.se/Lars/Gfit/html/index.html*

Freeland, S. L., Handy, B. N. 1998, Sol. Phys., 182, 497

Korendyke, C. M., Brown, C. M., Thomas, R. J., *et al.* 2006, Appl. Opt., 45, 8674

Kosugi, T., *et al.* 2007, Sol. Phys., submitted

Lang, J., Kent, B. J., Paustian, W., *et al.* 2006, Appl. Opt., 45, 8689

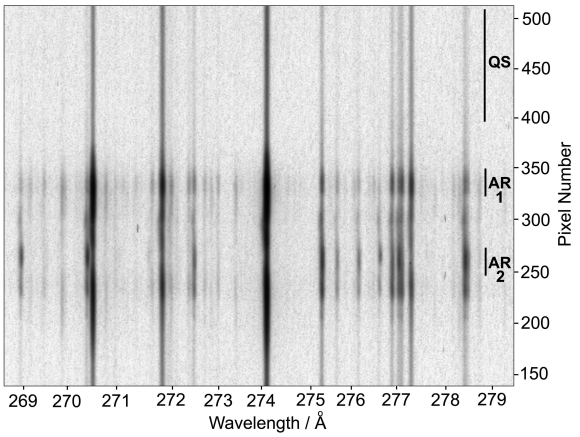

Fig. 1. Section of the EIS stigmatic spectrum spanning the 269 Å to 279 Å range. The quiet sun (QS) and two active areas (AR1, upper and AR2, lower) selected for the wavelength measurements are indicated.

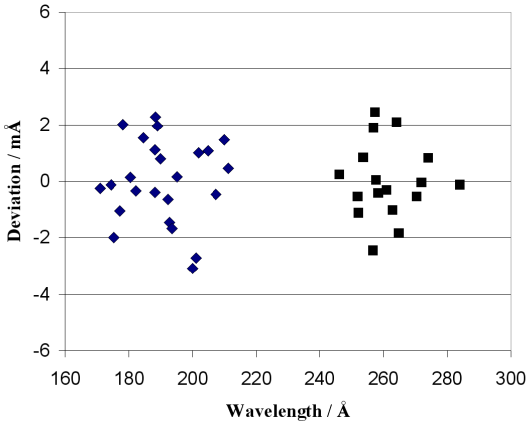

Fig. 2. Deviations of Behring et al. (1976) standards from EIS least squares fit. Only the "A" and "B" lines were used. The diamonds are data from the SW CCD and the squares are from the LW CCD.

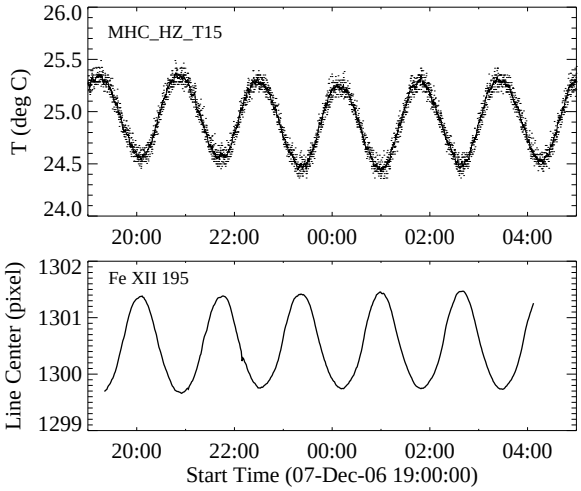

Fig. 3. Fe XII 195.12 Å line center variation over five orbits. The line center variation is well correlated with the temperature variation observed near the grating, with a small lag in the phase.

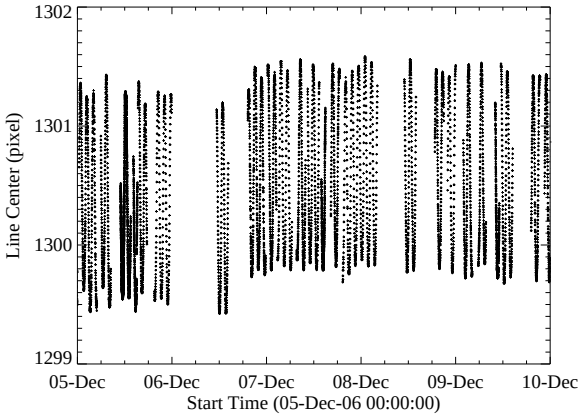

Fig. 4. Long term variation of Fe XII 195 Å line center. A net increase of 0.2 pixels in the average line center, equivalent to 7 km/s in velocity, occurs late on 6 December. It combines the effects of the sinusoidal orbital temperature variation with the thermal effects of Hinode repointing at 1100UT on 06 December 2006.

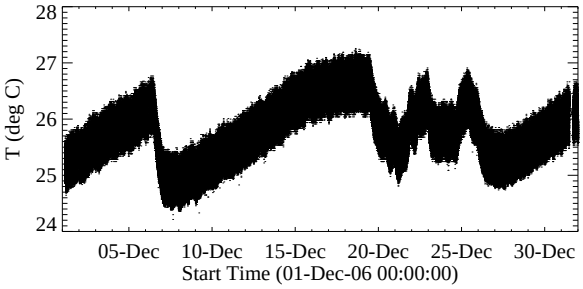

Fig. 5. A record of the EIS grating area temperature for the month of December, 2006.